Biosensors and Bioelectronics 132 (2019) 319–325

Contents lists available at ScienceDirect

Biosensors and Bioelectronics

journal homepage: www.elsevier.com/locate/bios

Development of highly sensitive H_2O_2 redox sensor from electrodeposited tellurium nanoparticles using ionic liquid

Manmohansingh Waldiya[a], Dharini Bhagat[a], Narasimman R[a], Shivam Singh[b], Arvind Kumar[c], Abhijit Ray[a], Indrajit Mukhopadhyay[a,*]

[a] Department of Solar Energy, School of Technology, Pandit Deendayal Petroleum University, Gandhinagar 382421, Gujarat, India
[b] Department of Physics, Indian Institute of Technology Bombay, Mumbai 400076, Maharashtra, India
[c] Salt and Marine Chemicals Division, Central Salt & Marine Chemicals Research Institute, Bhavnagar 364002, Gujarat, India

ARTICLE INFO

Keywords:
Tellurium nanoparticles
Electro deposition
Ionic liquid
Non-enzymatic sensor
Hydrogen peroxide
Excellent sensitivity

ABSTRACT

A new, non-enzymatic, low-cost sensor based on tellurium nanoparticles (TeNPs) for the analytical determination of H_2O_2 has been proposed. An economically viable electrochemical technique was employed for the synthesis of TeNPs based non-enzymatic H_2O_2 sensor. Thin films of TeNPs were successfully electrodeposited on fluorine-doped tin oxide (FTO) substrate using [BMIM][Ac] ionic liquid at 90 °C. The effect of deposition potential on the morphology, phase formation, and electrochemical characterisation of nanostructured Te films has been studied. Field emission scanning electron microscopy, X-ray diffraction, Raman and X-ray photoelectron spectroscopy were employed to characterize the nanostructured Te films on FTO surface. The electro-catalytic performance of the proposed TeNPs/FTO sensor has been studied by cyclic voltammetry (CV) and chronoamperometry (CA) in phosphate buffer (Argon saturated) in the absence and presence of H_2O_2. TeNPs/FTO fabricated at applied potential of −1.40 V showed an excellent electro-catalytic activity towards H_2O_2 reduction. The proposed TeNPs/FTO sensor shows an excellent sensitivity of 757 μA mM^{-1} cm^{-2}. The sensor possess good selectivity and stability with an excellent amperometric response time of about 5 s. The present study also demonstrates that TeNPs/FTO is a promising sensing material suitable for determination of H_2O_2 in practical samples.

1. Introduction

Non-enzymatic H_2O_2 electrochemical sensors have been well-studied as H_2O_2 is an important reactive oxygen species (ROS) that has direct relation to various biological processes. H_2O_2 is also a vital part in food and pharmaceutical industries as well as environmental, clinical and industrial research. It is of great importance to maintain the level of H_2O_2 as its deficiency may lead to various health problems viz cancer, Alzheimer's and Atherosclerosis diseases, and cardiovascular disorders. From earlier days, the detection and quantification of H_2O_2 remain a major challenge for many research groups in variety of fields, especially in cellular environments. In past decades to monitor levels of H_2O_2, the determination and quantification have been carried out using well-known techniques like chemiluminescent, colorimetric, fluorometric, spectrophotometry, volumetric and electrochemical analysis (Ghavamipour et al., 2018; Guascito et al., 2013; Manikandan et al., 2017; Wang et al., 2018). The analytical determination of H_2O_2 employing electrochemical technique has received much attention owing to the advantages associated with it as low-cost, wide linear range, lower detection limit, faster response and repeatability (Guzsvány et al., 2018; Manikandan et al., 2017).

Enzyme-based electrochemical sensors have gained much attention from earlier days as they possess the highest sensitivity and selectivity. However, owing to limitation of denaturation of enzymes, enormous efforts have been deployed for non-enzymatic amperometric sensors that possess excellent sensitivity and stability. Metal nanostructures based electrochemical sensors have the ability to decrease overpotential of many analysts (Guascito et al., 2013; Wang et al., 2017; Zong et al., 2018). Researchers have achieved excellent sensitivity and detectivity towards H_2O_2 for transition metal-based non-enzymatic electrochemical sensors. Nitrogen-doped carbon nanofibres showed high sensitivity of 357 μA $mM^{-1}cm^{-2}$ (Lyu et al., 2018). Guzsvany et al. have investigated the effect of AgNPs and AuNPs decorated multi-walled carbon nanotubes on amperometric detection of H_2O_2 (Guzsvány et al., 2018). The conditioned AuNPs on electrochemically derived graphene oxide showed high sensitivity of 741 μA mM^{-1} cm^{-2} towards H_2O_2

* Corresponding author.
E-mail address: indrajit.m@sse.pdpu.ac.in (I. Mukhopadhyay).

https://doi.org/10.1016/j.bios.2019.02.050
Received 14 December 2018; Received in revised form 13 February 2019; Accepted 28 February 2019
Available online 02 March 2019
0956-5663/

(Berbeć et al., 2018). In such context, Tellurium (Te) is p-type (E_g ~ 0.35 eV) semiconductor with excellent electrochemical, thermoelectric, nonlinear optical and sensing properties (Guascito et al., 2011; Piacenza et al., 2018). Depending on shape and size, Te possesses applications in sensors, optoelectronic devices, photovoltaics and supercapacitors (Piacenza et al., 2018). From decades, Te nanostructures have been fabricated using different techniques viz hydrothermal, microwave assisted, electrochemical (Piacenza et al., 2018; Zhu et al., 2004) and many more. The use of Te nanostructures to determine and quantify level of H_2O_2 is also a well-investigated topic (Erande and Late, 2016; Guascito et al., 2011; Manikandan et al., 2017; Manjare et al., 2014; Saini et al., 2018). In order to create next generation of smart functional materials, the ability to align nanostructures onto numerous substrates is of utmost importance. Fluorine doped tin oxide (FTO) is an economically viable transparent conducting oxide (TCO) substrate suitable in numerous applications including sensors, thin film solar cells and in liquid crystal displays (Hecht et al., 2011). However, the electrochemical synthesis of Te nanostructures using "Green" solvents onto TCO and their subsequent use as H_2O_2 sensing is still not explored. The advantages offered by "Green" solvent, ionic liquids (ILs) include good ionic mobility, low vapour pressure, wide electrochemical window, and high chemical and thermal stability.

Here, we present for the first time the electrochemical synthesis of low-cost tellurium nanoparticles (TeNPs) onto FTO substrate using air- and water-stable ionic liquid. Further, the influence of deposition potential on surface morphology and electrocatalytic performance of TeNPs have been studied. The novelty of the work includes the fabrication of economically viable non-enzymatic electrochemical H_2O_2 sensor based on electrodeposited TeNPs (TeNPs/FTO).

2. Material and methods

2.1. Synthesis of tellurium nanoparticles (TeNPs)

TeNPs were synthesized directly onto FTO substrate using electrodeposition technique at 90 °C. Ionic liquid (IL), 1-butyl-3-methylimidazolium acetate ([BMIM][Ac]) was used as the green solvent for electrochemical process. A conventional three-electrode system comprising of FTO (~ 7 Ω/sq, Aldrich, 0.25 cm^2) served as the working electrode (WE) with platinum (Pt) wire and mesh as pseudo reference electrode (RE) and counter electrode (CE), respectively. The cleaning process of FTO substrate includes subsequent ultrasonication in trichloroethylene, iso-propanol, acetone and de-ionised water for 15 mins each. Tellurium oxide (5 mM TeO_2, 99%) was used as the precursor source. Solvent and precursor were purchased from Aldrich (Bangalore, India) and used as received. Cathodic deposition of TeNPs on FTO was carried out at three different applied potentials: −1.30, −1.40, and −1.50 V (vs Pt wire). Due to the limited solubility of TeO_2 in [BMIM][Ac], the bath temperature was kept constant at 90 °C for each deposition parameter.

Cyclic Voltammetry (CV) and Chronoamperometry (CA) were carried out using potentiostat/galvanostat (PGSTAT302N, Autolab) to study the electrochemical process involved in Te deposition. FE-SEM (Ultra-55, Zeiss) and Powder X-ray Diffraction (X'pert Pro, PANalytical) were used to determine the surface morphology and crystal structure of TeNPs. The electrodeposited TeNPs on FTO surface were further characterized by Raman spectroscopy (Renishaw micro-raman, inVia) and XPS (AXIS Supra, Kratos Analytical, United Kingdom).

2.2. Electrochemical characterisation of TeNPs/FTO non-enzymatic sensor

A three electrode setup was used for the investigation of non-enzymatic electrochemical sensing behaviour. FTO modified with electrodeposited TeNPs (TeNPs/FTO) was used as WE, Pt mesh as CE, and Ag/AgCl as RE. All measurements were performed on potentiostat/galvanostat (PGSTAT302N, Autolab). Phosphate buffer (pH 7) was used as the electrolyte for all voltammetric and amperometric experiments. The buffer was deoxygenated with bubbling of Argon gas for about an hour prior electrochemical measurements. CV and CA studies were performed to determine the sensitivity, selectivity, stability and detection limit of fabricated TeNPs/FTO non-enzymatic sensor towards H_2O_2.

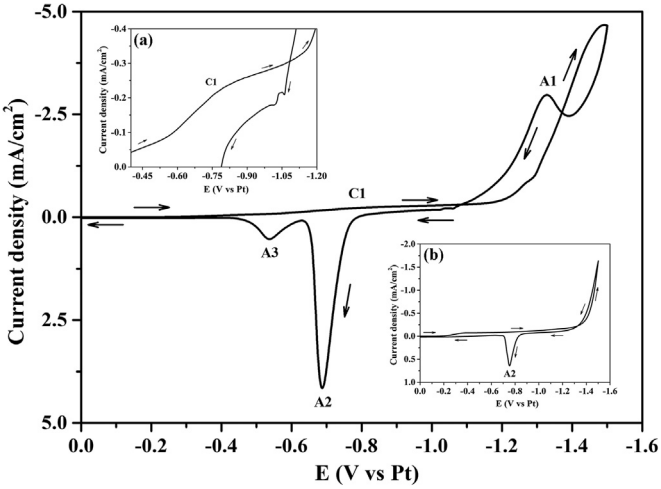

Fig. 1. Cyclic Voltammogram for the electrodeposition of Te from TeO_2 in [BMIM][Ac] at sweep rate of 25 mV/s at 90 °C.

3. Results and discussion

3.1. Deposition of TeNPs by electrochemical method

Typical cyclic voltammogram (CV) for the electrodeposition of TeNPs on FTO substrate is shown in Fig. 1. Potentiostat/Galvanostat was used to record CV for electrochemical deposition of Te containing 5 mM TeO_2 in [BMIM][Ac] at sweep rate of 25 mV/s at 90 °C. As such no distinguishable cathodic peaks have been observed. However, a closer look at the CV curve (Fig. 1 *Inset a*) shows a current hump in the potential range from −0.60 to −1.15 V. The broad hump, C1 is associated to under-potential deposition (UPD) of Te species onto FTO substrate (Waldiya et al., 2018), followed by an increase in cathodic current at around −1.15 V. The negative current continue to rise at −1.15 V, which may be referred to as the starting of overpotential deposition (OPD) regime of Te species. Furthermore, a current loop due to three-dimensional (3D) nucleation and growth of Te on FTO substrate is well observed at extreme cathodic potential. Whereas in the anodic scan, current hump, A1 (-1.32 V) is attributed to the oxidation of adsorbed Te species (Jaya et al., 1986; Nguyen et al., 2013). The existence of Te monolayer on FTO substrate can be confirmed as plot linearity is observed for the plots between E_p^{-2} vs I_p (Fig. SI-1) and $Ln\ \nu$ vs E_p (Fig. SI-2) (Jaya et al., 1986). The current hump, A2 (−0.69 V) may be associated to the oxidation of unbound water molecule or anionic species of ionic liquid as also observed in the case for CV study in blank IL (Fig. 1 *Inset b*). Finally, current hump, A3 (−0.54 V) is due to the stripping of Te species onto the solution.

Elemental Te was electrodeposited onto FTO substrate from acetate-based ionic liquid bath at three different applied potentials. The potentials viz. −1.30, −1.40, and −1.50 V (vs Pt wire) were located in the OPD region as illustrated from CV (Fig. 1). Generally, the early stages of electrodeposition of metal involves phase formation of species on foreign substrate in well-defined 2D and/or 3D nucleation and growth processes (Scharifker and Hills, 1983). Fig. 2 shows current-time (*I-t*) transients obtained for three applied overpotentials. It can be observed from *I-t* curves that there is an unambiguous decrease in the initial current for shorter time domain due to double layer discharge.

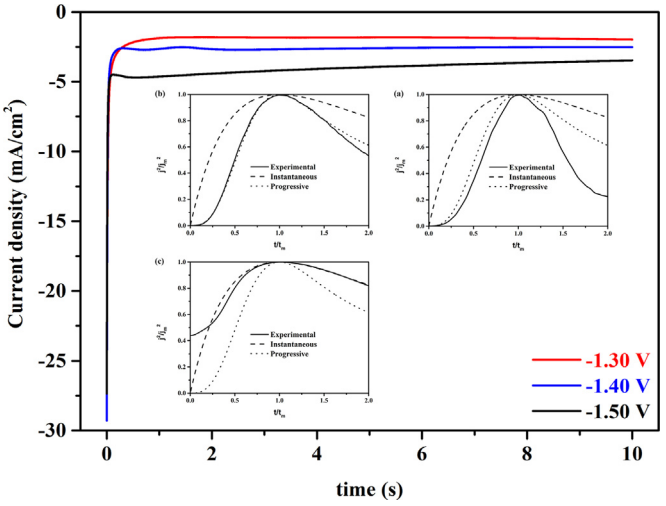

Fig. 2. Current transients of electrodeposited TeNPs recorded on FTO substrate. ***Inset***: Non-dimensional plot for 3D process showing comparison between experimental and theoretical curves (**a**) −1.30 V (b) −1.40 V (c) −1.50 V.

Further, rise in current density is seen due to the formation of increased electroactive area and overlapping of nuclei, followed by an exponential decrease owing to linear diffusion of species on the already formed nuclei. Moreover, it can be observed that current transients pass through the current maxima (I_m) and the time (t_m) corresponding to I_m decreases with more applied cathodic overpotentials (Fig. SI-3).

In order to further understand the nucleation and growth mechanism involved in deposition of TeNPs on FTO substrate, current transients were fitted using the theoretical Scharifker and Hills (S-H) model (Scharifker and Hills, 1983). *I-t* curves obtained theoretically using below equations, along with the experimental plots are illustrated in *inset* of Fig. 2.

For instantaneous (3D)

$$\left(\frac{I}{I_m}\right)^2 = \frac{1.9542}{(t/t_m)}\left[1-exp\left(-1.2564\frac{t}{t_m}\right)\right]^2 \quad (1)$$

For progressive (3D)

$$\left(\frac{I}{I_m}\right)^2 = \frac{1.2254}{(t/t_m)}\left[1-exp\left(-2.3367\frac{t^2}{t_m^2}\right)\right]^2 \quad (2)$$

where, I_m is current maximum and t_m is time at which maximum current is observed. It is observed that at applied potential of −1.30 V (Fig. 2 *Inset a*), the transient shows near to progressive nucleation and growth mechanism while an exact progressive mechanism is observed with increase in the overpotential to −1.40 V (Fig. 2 *Inset b*). This fact is evident from FE-SEM micrographs (Fig. 3c) where the evolution of broad size distribution of nanoparticles is associated with progressive mode of nucleation and growth. However, current transient at −1.50 V is in well agreement with the theoretical instantaneous growth model (Fig. 2 *Inset c*). Here, the density of nuclei remains almost unchanged although the growth occurs at higher rate which is evident from the growth of lumps on the already formed TeNPs (Fig. 3d). More aspects to talk about the size distribution that follow 3D nucleation and growth model is not discussed owing to the restriction of the theme of the paper.

3.2. Morphological and structural analysis of Te NPs

FE-SEM images of pristine FTO and electrochemically deposited TeNPs on FTO at different applied potential are shown in Fig. 3. In all cases, deposits of nanostructured Te can be seen. A narrow size distribution of TeNPs is seen when deposition was carried at lower overpotential of −1.30 V, however substantial fraction of substrate surface is also seen uncovered due to less nuclei density (Fig. 3b). When the electrodeposition was carried out at −1.40 V, the density of TeNPs increases and complete coverage of FTO surface was observed. Here, broad size distribution of TeNPs is seen along with agglomerated lumps on the already formed nuclei (Fig. 3c). In the case when deposition was carried out at more negative overpotential (−1.50 V, Fig. 3d), the substrate gets fully covered with Te deposits, however, the particles losses its peripheral shape (spherical) as they diffuse onto one another. Also, the lumps grown over the already deposited nanoparticles increase in size.

The phase analysis of TeNPs was studied by X-Ray Diffraction. XRD pattern of the electrodeposited TeNPs using [BMIM][Ac] ionic liquid at 90 °C are shown in Fig. 4a. The diffraction peak for all samples fit well with the monoclinic phase (space group *C*12/*m*1) of tellurium (COD 2016 # 96-153-3531). At OPD of −1.30 V, the preferential orientation (*PO*) is at 2θ = 37.8° due to the reflection from (310) plane. However, the *PO* shifts to 2θ = 30.7°, for OPD of −1.40 and −1.50 V, which is the characteristic peak of monoclinic Te with reflection in (-111) plane (Takumi et al., 2002). Some of the impurity peaks of Sn (tin) and SnTe (tin telluride) were also observed. This may have happened due to the sensitization (superficial cathodic reduction) of SnO_2 to Sn that may have oxidized to SnTe in the deposition solution prior to electrodeposition (Kampmann et al., 1995).

The crystallite size of Te deposits were determined using the Debye Scherrer's equation:

$$D = \frac{0.9\ \ \lambda}{\beta cos\theta} \quad (3)$$

where, β is full width at half maximum (FWHM) of the diffraction peak, λ is wavelength of X-rays (Cu k_α = 1.5406 Å), θ is the Bragg angle and k is the Scherrer constant. The average crystallite size of TeNPs is nearly same when deposition was carried out at −1.30 V(24.44 nm) and −1.40 V (24.70 nm). However, for OPD at −1.50 V, the average crystallite size increases to 28.94 nm.

We further characterize the electrodeposited TeNPs using Raman spectroscopy. Raman scattering can provide information about the molecular structure (Ntholeng et al., 2016). The Wire4 software was used to record the Raman spectra and Lorentz function was used to fit the peak positions in order to obtain the phonon wavenumbers. The Raman spectrum of bulk Te at room temperature is dominated by two set of modes: A1 singlet at 120 cm^{-1} and a pair of E doublets at 92 (104) and 141 (141) cm^{-1} for transverse (longitudinal) phonons (Brodsky et al., 1972; Churchill et al., 2017). Fig. 4b shows Raman spectra of TeNPs on FTO substrate at room temperature with an excitation wavelength of 532 nm. The two strong peaks at around 122 and 141 cm^{-1} are attributed to A1 and E phonon mode of vibration for pure Te. At OPD at −1.30 V, the spectrum shows strong peak at 112 cm^{-1} that may be associated to E (transverse) phonon mode. However, a peak broadening in wavenumber range of 115–175 cm^{-1} was also observed. The peak at 210 cm^{-1} is the vibrational mode from sensitized SnO_2 surface (Fig. 4b). When deposition was carried out at more cathodic potentials, the A1 singlet at 122 and 123 cm^{-1} was observed for OPD at −1.40 and −1.50 V, respectively. Similar shift in E vibrational mode was also observed with peak positioned at 141 (−1.40 V) and 142 (−1.50 V) cm^{-1}. Here, no peaks of sensitized SnO_2 were observed. It was observed that with decrease in the deposition potential from −1.50 to −1.30 V, the softening in Raman peak occurs. The softening of phonons usually follows when the material undergoes phase transition (Venkataraman, 1979). Thus, Raman study illustrates the formation of pure TeNPs in all cases.

Now we correlate the change in *PO* in XRD peak with that of Raman spectrum. As *PO* in the case for −1.40 and −1.50 V is at 30.7° (Fig. 4a), the Raman spectra shows strong A1 singlet mode at 122 and 123 cm^{-1} (Fig. 4b), respectively. The singlet A1 mode is described as the

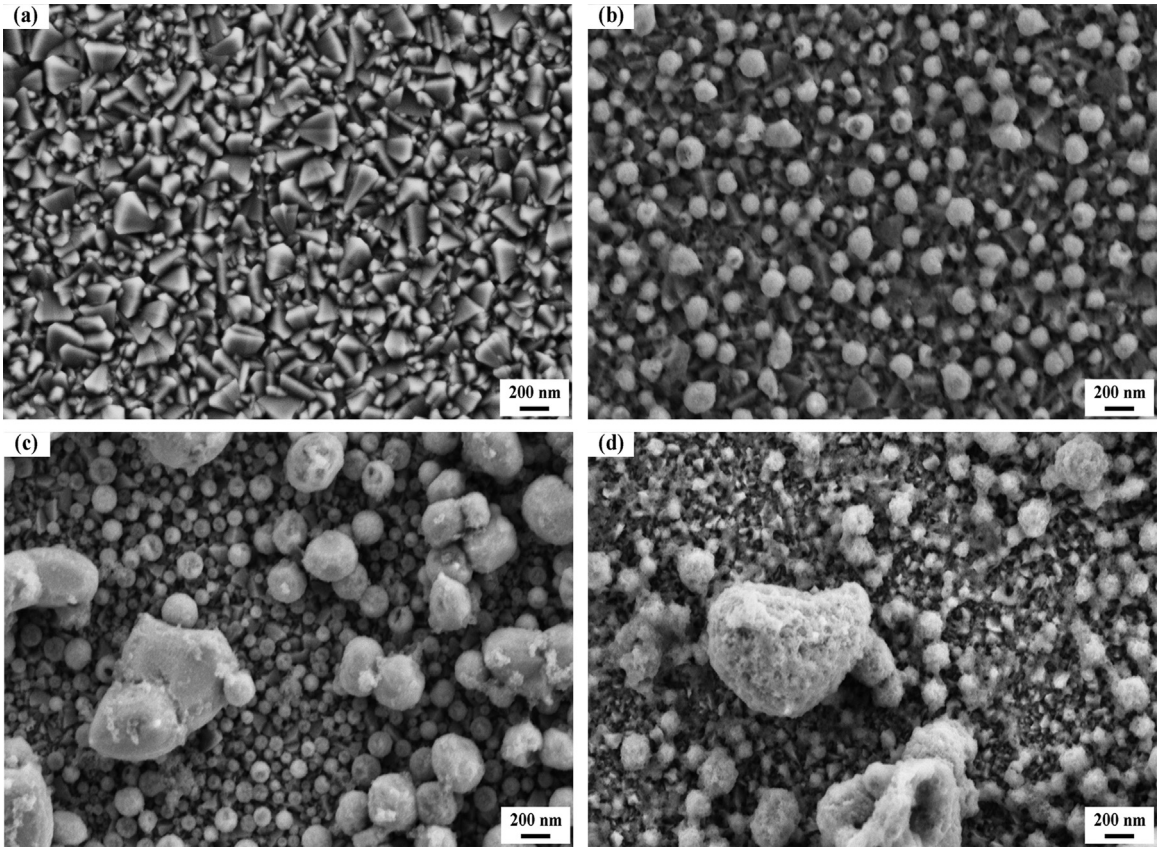

Fig. 3. FE-SEM images of TeNPs electrochemically deposited at different applied potentials onto FTO substrate using [BMIM][Ac] at 90 °C. (**a**) Pristine FTO (**b**) −1.30 V (**c**) −1.40 V (**d**) −1.50 V; deposition time: 600 s.

symmetric mode with respect to C_2 axis that is perpendicular to the principal axis (Tuschel, 2014). However, for OPD at −1.30 V, the *PO* changes to 37.8° (Fig. 4a), and as a result, a less active A1 mode is observed (Fig. 4b).

Furthermore, to study the states of TeNPs over FTO, XPS measurements were carried out using monochromatic Al K-alpha (normally 75W). The details of high-resolution XPS (HR-XPS) spectra (3d), providing details of the near surface chemistry of TeNPs adsorbed on FTO surface, is shown in Fig. 4c and SI-4. The energy scales of XPS data are corrected for peak positions referenced to aliphatic C 1s, as an internal standard, set at 284.8 eV (Guascito et al., 2013). XPSpeak software was used for data analysis and de-convolution of the peaks. HR-XPS of TeNPs/FTO exhibits two main single peaks at 583.4 ± 0.1 and 573.0 ± 0.1 recorded in all cases were attributed to Te^0 $3d_{5/2}$ and Te^0 $3d_{3/2}$, respectively, for the metallic state of Te. The peak component at lower BE (579.5 ± 0.1) can be associated to Te mixed oxides of surface (Guascito et al., 2013). Fig. 4d shows HR-XPS spectrum of TeNPs after being subject to multiple voltammetric cycles in phosphate buffer (pH 7). It can be observed that the peak component at lower BE disappears after multiple CV measurements. These data confirms that species of tellurium involved in CV experiments are Te(0) and mixed oxides of Te in the present experimental conditions.

3.3. Electrochemical sensing of H_2O_2

CV was used to study the electrochemical property of TeNPs/FTO sensor towards H_2O_2. The performance of TeNPs/FTO fabricated from acetate-based IL bath at different applied overpotentials has been evaluated in deoxygenated phosphate buffer (PB; pH 7). Fig. 5a shows CV plots of TeNPs/FTO synthesized at different OPD (viz. −1.30 to −1.50 V vs Pt wire) in argon saturated PB at scan rate of 40 mV/s. In the pH range from 1.93 to 8.36, Te precipitates as TeO_2 (Guascito et al., 2011). Apparently redox process involved in the oxidation and subsequent reduction of TeNPs can be observed. TeNPs/FTO electrode show anodic peaks (E_{pa}) at 0.23 and 0.79 V (−1.30 V), 0.19 V (−1.40 V), 0.24 and 0.81 V (−1.50 V), while the subsequent cathodic peaks (E_{pc}) were observed at −0.45 and −0.65 V (−1.30 V), −0.45 and −0.79 V (−1.40 V), −0.41 and −0.62 V (−1.50 V). According to CV measurements and XPS analysis, the mechanism of sensing that involves peak pair TeO_2/Te adsorbed over FTO, can be explained as follows (Guascito et al., 2011, 2013; Manikandan et al., 2017):

$$Te + 2H_2O \leftrightarrow TeO_2 + 4H^+ + 4e^- \ (E_{pa}\sim 0.20\ V \text{ in oxidation}) \quad (4)$$

$$TeO_2 + 4H^+ + 4e^- \leftrightarrow Te + 2H_2O + 2O_2\ (E_{pc}\sim -0.45\ V \text{ in reduction}) \quad (5)$$

It can be observed that FTO modified with TeNPs decreases the red/ox potential of Te at pH 7 (Manikandan et al., 2017). The sensing mechanism involves four electron transfer process. Further, to determine the dynamic characteristics of TeNPs/FTO electrodes, CV were recorded at different scan rates in the potential range −1.20 to + 1.50 V (Vs Ag/AgCl). The graph of peak current (I_p) vs. scan rate (υ) and I_p vs. Log υ show linear dependency with increase in scan rate, which suggests surface adsorption-controlled electrode process (Fig. SI-5). Fig. SI-6 show CV curves of TeNPs/FTO in buffer with absence and presence of H_2O_2 at scan rate of 40 mV/s. It can be observed that upon addition of H_2O_2, TeNPs/FTO exhibits significant rise in anodic and cathodic peak currents. TeNPs/FTO fabricated at OPD of −1.40 V (Fig. SI-6b) shows highest current density during anodic as well as cathodic scans in absence and presence of H_2O_2 in phosphate buffer. This infers that TeNPs/FTO has excellent electrochemical properties, which may be because of densely packed TeNPs over FTO surface. As expected, the current density of TeNPs/FTO fabricated at −1.40 V further increases with increase in H_2O_2 concentration (Fig. 5b). This illustrates

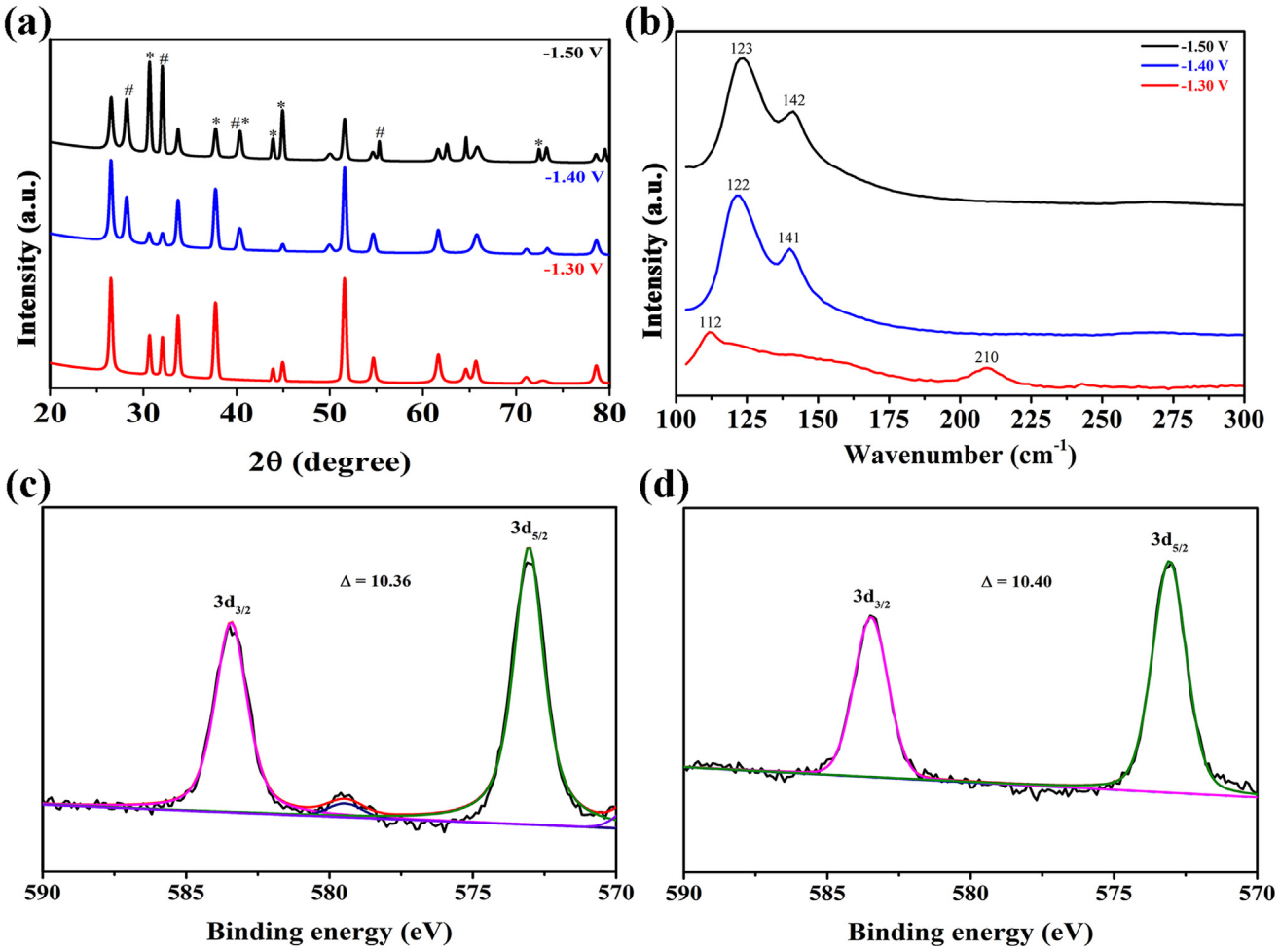

Fig. 4. (**a**) XRD pattern of electrodeposited TeNPs at different OPDs. (Te *; Sn #; SnTe #*; substrate peaks: unmarked). (**b**) Raman scattering of TeNPs with excitation wavelength of 532 nm at room temperature. HR-XPS spectra of TeNPs electrodeposited at OPD of −1.40 V: (**c**) as synthesized and (**d**) after 30 CV cycles.

improvement in the surface activation and faster electron transfer between TeNPs and H_2O_2. Fig. SI-7a shows cathodic peak current plotted with respect to H_2O_2 concentration for TeNPs/FTO (−1.40 V). The cathodic peak current increases linearly with increase in H_2O_2 concentration that shows an excellent electrocatalytic activity of TeNPs/FTO towards H_2O_2 reduction.

The amperometric response of TeNPs/FTO prepared at different OPD upon successive addition of H_2O_2 (100 μM) in buffer (pH 7) measured at applied potential of −0.50 V (Vs Ag/AgCl) is shown in Fig. 5c. We can clearly observe that TeNPs/FTO fabricated at −1.40 V shows enhancement in the current response towards H_2O_2 as compared to TeNPs electrodeposited at −1.30 and −1.50 V (vs Pt wire). CV and CA studies match well with one another. *I-t* curve possess a steady-state transient response within 5 s upon H_2O_2 addition in stirred PB. Fig. SI-7c illustrates *I-t* response of TeNPs/FTO (−1.40 V) measured at two different potentials −0.25 and −0.50 V. The corresponding calibration curve is shown in Fig. 5d. It is well known that the sensitivity of an electrochemical sensor is highly influenced by applied potential in chronoamperometry (Zhang et al., 2018). Fig. SI-7b and SI-7d shows *I-t* response of TeNPs/FTO fabricated at two different OPDs (−1.30 and −1.50 V) measured at two different potentials (−0.25 and −0.50 V), respectively. As expected the sample shows enhancement in the sensitivity when the calibration curve was measured at −0.50 V (vs Ag/AgCl). The sensitivity of TeNPs/FTO electrodeposited at −1.40 V (vs Pt wire) is 0.757 mA mM^{-1} cm^{-2} measured at −0.50 V (vs Ag/AgCl) in the linear range 0.10–0.50 mM (correlation coefficient 0.995). The limit of detection (LOD) was estimated to be 28.4×10^{-6} M (S/N = 3). However, the sensitivity and LOD of the same sample measured at −0.25 V is 0.167 mAm$M^{-1}$$cm^{-2}$ and 33.2×10^{-6} M, respectively (correlation coefficient 0.992). Fig. 5e shows the sensitivity of TeNPs/FTO sensors. The excellent sensitivity and low detection limit of TeNPs/FTO can be associated with densely packed nanoparticles that show improvement in surface activation energy with faster electron transfer kinetics (Figs. 3 and 5). The lowest sensitivity was found to be 0.126 mA mM^{-1} cm^{-2} for TeNPs/FTO fabricated at −1.30 V (vs Pt wire). Fig. SI-7e illustrates *I-t* response of TeNPs/FTO (−1.40 V) measured at −0.50 V in the linear range 20 μM to 2 mM H_2O_2 in buffer. Thus, we can conclude that the proposed TeNPs/FTO sensor has wide dynamic concentration range.

Furthermore, the selectivity and stability of TeNPs/FTO sensor (−1.40 V) were also determined using phosphate buffer (pH 7). The sensitivity was determined by monitoring *I-t* response under successive injection of 100 μM each of H_2O_2 and other interfering species viz. D-glucose, D-fructose, Sucrose, Lactic Acid and Ascorbic Acid measured at −0.50 V (vs Ag/AgCl). The selectivity of TeNPs/FTO sensor towards H_2O_2 is illustrated in Fig. 5f. TeNPs/FTO sensor shows remarkable amperometric response towards H_2O_2 reduction. However, the sensor does not exhibit significant change in cathodic current upon addition of other interfering species. This indicates excellent selectivity of the proposed sensor. The stability of TeNPs/FTO was evaluated by CV, repeated for 25 cycles in 1 mM H_2O_2 in PB. As such, no alteration in peak potential and peak current was observed for reduction of H_2O_2 (Fig. SI-7f). Fig. SI-7f *(inset)* shows *I-t* response of TeNPs/FTO sensor after multiple CV measurements. This confirms high stability of the

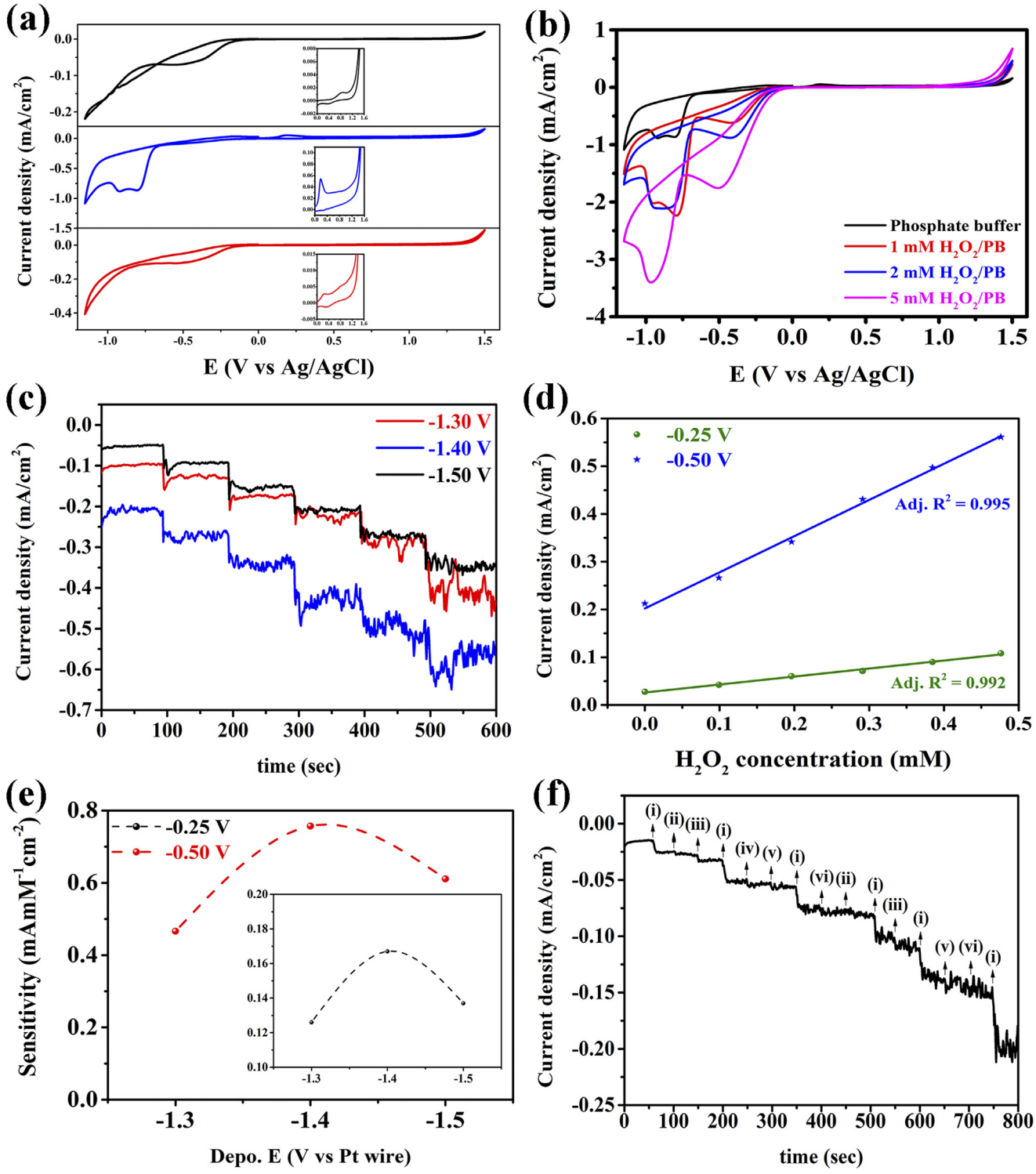

Fig. 5. (**a**) CV of TeNPs/FTO in Argon saturated buffer pH 7. ***Inset*:** CV plot in anodic potential range. (**b**) CV of TeNPs/FTO fabricated at −1.40 V in absence and presence of H_2O_2 in phosphate buffer. (**c**) *I-t* response of TeNPs/FTO upon successive addition of 100 μM H_2O_2 in buffer measured at −0.50 V. (**d**) Plot for the corresponding calibration curve (-1.40 V). (**e**) Sensitivity of the proposed TeNPs/FTO sensor. (**f**) Selectivity of the proposed TeNPs/FTO sensor (i) H_2O_2 (ii) D-glucose (iii) D-fructose (iv) Sucrose (v) Lactic Acid (vi) Ascorbic Acid.

proposed sensor. Table SI-1 describes the comparison of various modified H_2O_2 sensor with the present study. It can be seen that TeNPs based low-cost sensor is in comparable range to recent reported H_2O_2 sensors.

Finally, the feasibility of the fabricated TeNPs/FTO sensors was conducted in milk as the real sample. It is well known that H_2O_2 has been widely used as a preservative (0.05–0.25%) in commercial production due to its bactericidal properties. However, excess of H_2O_2 can have an adverse effect on the nutritional values of milk. The analytical applicability of the sensor was evaluated by calibration curve method to determine the recoveries for different concentration of H_2O_2 in sterilized milk (Lyu et al., 2018). The milk samples were prepared upon successive addition of H_2O_2 to 5.0 ml milk solution containing 0.5 ml of commercial milk and 5.0 ml of buffer (pH 7; Argon saturated).

Table 1
Determination of H_2O_2 in Milk samples.

Added H_2O_2 (μM)	Detected H_2O_2 (μM)	R.S.D. (%)	Recovery (%)
0	–	–	–
100	108.5	4.52	108.5
200	191.1	5.80	95.5
300	282.3	3.98	94.1

The results calculated based on regression equation obtained from Fig. SI-8 are summarised in Table 1. The high recovery and low-relative standard deviation (RSD) as obtained from three measurements conclude that the fabricated low-cost TeNPs/FTO sensor can be employed for sensitive and selective detection of H_2O_2 in Real samples.

4. Conclusions

To summarize, we have synthesized highly dense thin films of spherical Te nanoparticulate on FTO surface using ionic liquid by low-cost electrochemical technique. Te shows nanoparticle-like morphology following 3D nucleation and growth mechanism. The deposition at −1.40 V (vs Pt wire) leads to the formation of densely packed nanoparticles having high surface energy. The shift in Raman peak can be correlated to phase transformation in TeNPs. We have demonstrated that TeNPs/FTO electrode exhibits lower overpotential for oxidation and reduction of H_2O_2 in buffer (pH 7). Non-enzymatic amperometric sensor based on TeNPs/FTO shows excellent sensitivity of 757.4 μA/cm^{2}mM due to densely packed substrate surface. The proposed sensor material also possesses high selectivity and better stability to be useful in sensor and biosensor applications. The present study also demonstrates that TeNPs/FTO sensor find its potential as an electrochemical sensing material in practical applications. We believe that sensor properties can further be enhanced by doping with other elements and/or using different foreign substrates.

CRediT authorship contribution statement

Manmohansingh Waldiya: Data curation, Formal analysis, Investigation, Methodology, Validation, Visualization, Writing - original draft, Writing - review & editing. **Dharini Bhagat:** Formal analysis, Writing - original draft, Writing - review & editing. **Narasimman R:** Formal analysis, Writing - original draft. **Shivam Singh:** Formal analysis. **Arvind Kumar:** Resources. **Abhijit Ray:** Formal analysis. **Indrajit Mukhopadhyay:** Conceptualization, Supervision.

Acknowledgements

Authors would like to acknowledge Solar Research & Development Centre and Pandit Deendayal Petroleum University for providing financial and technical assistance. Authors would also like to acknowledge Central Surface Analytical Facility of IIT Bombay for providing XPS measurements.

Compliance with ethical standards

Author(s) have no competing interests.

Declaration of interests

None.

Appendix A. Supporting information

Supplementary data associated with this article can be found in the online version at doi:10.1016/j.bios.2019.02.050.

References

Berbeć, S., Żołądek, S., Jabłońska, A., Pałys, B., 2018. Sens. Actuators B: Chem. 258, 745–756.
Brodsky, M.H., Gambino, R.J., Smith Jr, J.E., Yacoby, Y., 1972. Phys. Status Solidi (b) 52 (2), 609–614.
Churchill, H.O.H., Salamo, G.J., Yu, S.-Q., Hironaka, T., Hu, X., Stacy, J., Shih, I., 2017. Nanoscale Res. Lett. 12 (1), 488.
Erande, M.B., Late, D.J., 2016. Adv. Device Mater. 2 (1), 8–14.
Ghavamipour, F., Sajedi, R.H., Khajeh, K., 2018. Microchim. Acta 185 (8), 376.
Guascito, M.R., Chirizzi, D., Malitesta, C., Mazzotta, E., Siciliano, M., Siciliano, T., Tepore, A., Turco, A., 2011. Biosens. Bioelectron. 26 (8), 3562–3569.
Guascito, M.R., Chirizzi, D., Malitesta, C., Siciliano, T., Tepore, A., 2013. Talanta 115, 863–869.
Guzsvány, V., Vajdle, O., Gurdeljević, M., Kónya, Z., 2018. Top. Catal. 1–12.
Hecht, D.S., Hu, L., Irvin, G., 2011. Adv. Mater. 23 (13), 1482–1513.
Jaya, S., Prabhakarrao, G., Prasadarao, T., 1986. Bull. Electrochem. 2 (1), 65–68.
Kampmann, A., Cowache, P., Mokili, B., Lincot, D., Vedel, J., 1995. J. Cryst. Growth 146 (1–4), 256–261.
Lyu, Y.-P., Wu, Y.-S., Wang, T.-P., Lee, C.-L., Chung, M.-Y., Lo, C.-T., 2018. Microchim. Acta 185 (8), 371.
Manikandan, M., Dhanuskodi, S., Maheswari, N., Muralidharan, G., Revathi, C., Kumar, R.T.R., Rao, G.M., 2017. Sens. Bio-Sens. Res. 13, 40–48.
Manjare, S.T., Kim, Y., Churchill, D.G., 2014. Acc. Chem. Res. 47 (10), 2985–2998.
Nguyen, T.G.H., Pham, T.V.A., Phuong, T.X., Lam, T.X.B., Nguyen, T.P.T., 2013. Adv. Nat. Sci.: Nanosci. Nanotechnol. 4 (3), 035008.
Ntholeng, N., Mojela, B., Gqoba, S., Airo, M., Govindraju, S., Moloto, M.J., Van Wyk, J., Moloto, N., 2016. New J. Chem. 40 (12), 10259–10266.
Piacenza, E., Presentato, A., Zonaro, E., Lampis, S., Vallini, G., Turner, R.J., 2018. Phys. Sci. Rev. 3 (5).
Saini, N., Goyal, S., Narula, C., Chauhan, R.P., 2018. J. Mater. Sci. Mater. Electron. 29 (19), 16673–16679.
Scharifker, B., Hills, G., 1983. Electrochim. Acta 28 (7), 879–889.
Takumi, M., Masamitsu, T., Nagata, K., 2002. J. Phys.: Condens. Matter 14 (44), 10609.
Tuschel, D., 2014. Spectroscopy 29 (2), 14.
Venkataraman, G., 1979. Bull. Mater. Sci. 1 (3–4), 129–170.
Waldiya, M., Bhagat, D., Mukhopadhyay, I., 2018. J. Electroanal. Chem. 814, 59–65.
Wang, N., Duan, J., Shi, W., Zhai, X., Guan, F., Yang, L., Hou, B., 2018. Microchim. Acta 185 (9), 417.
Wang, Z., Cao, X., Liu, D., Hao, S., Kong, R., Du, G., Asiri, A.M., Sun, X., 2017. Chem. Eur. J. 23 (21), 4986–4989.
Zhang, W., Fan, G., Yi, H., Jia, G., Li, Z., Yuan, C., Bai, Y., Fu, D., 2018. Small 14 (19), 1703713.
Zhu, Y.J., Wang, W.W., Qi, R.J., Hu, X.L., 2004. Angew. Chem. 116 (11), 1434–1438.
Zong, C., Li, B., Wang, J., Liu, X., Zhao, W., Zhang, Q., Nie, X., Yu, Y., 2018. Microchim. Acta 185 (3), 199.